Tri-sulfur radical trapping in lithium–sulfur batteries

Journal of Power Sources Advances 28 (2024) 100153

Contents lists available at ScienceDirect

Journal of Power Sources Advances

journal homepage: www.sciencedirect.com/journal/journal-of-power-sources-advances

Tri-sulfur radical trapping in lithium–sulfur batteries

Roza Bouchal [a,*], Clément Pechberty [a], Athmane Boulaoued [a], Niklas Lindahl [a,b], Patrik Johansson [a,c]

[a] Department of Physics, Chalmers University of Technology, 412 96, Gothenburg, Sweden
[b] Department of Physics, Gothenburg University, 412 96, Gothenburg, Sweden
[c] ALISTORE-ERI, CNRS, FR 310, Hub de l'Energie, 80039, Amiens, France

ARTICLE INFO

Keywords:
Li-S batteries
Tri-sulfur radical
Radical trap
Cycling stability

ABSTRACT

Lithium-sulfur (Li–S) batteries have emerged as a next-generation battery technology owing to their prospects of high capacity and energy density. They, however, suffer from rapid capacity decay due to the shuttling of reaction intermediate species: Li polysulfides (LiPSs). One of the more important and intriguing PSs is the tri-sulfur radical ($S_3^{\bullet-}$), observed mainly in high-donor number (DN) solvent-based electrolytes. Although this radical has been proposed to be crucial to full active material (AM) utilization, there is currently no direct evidence of the impact of $S_3^{\bullet-}$ on cycling stability. To gain more insight into the role of the $S_3^{\bullet-}$, we studied the use of radical traps in low and high DN solvent-based electrolytes by *operando* Raman spectroscopy. The traps were based on nitrone and iminium cation, and $S_3^{\bullet-}$ was indeed successfully trapped in *ex situ* analysis. However, it was the ionic liquid-based trap, specifically pyridinium, that effectively suppressed $S_3^{\bullet-}$ during battery operation. Overall, the PS formation was altered in the presence of the traps and we confirmed the impact of $S_3^{\bullet-}$ formation on the Li–S battery redox reactions and show how the trapping correlates with Li–S battery performance. Therefore, stabilization of the $S_3^{\bullet-}$ might be a path to improved Li–S batteries.

1. Introduction

Li–S batteries are considered a promising alternative/complement to the current dominant lithium-ion battery (LIB) technology, and if successful it will support the fast-expanding energy storage demand [1,2]. Sulfur is a very cheap, non-toxic and naturally abundant element. It is used as the cathode active material (AM) in a mixture with carbon, in order for the electrode to be electrically conductive. Combining this cathode with a high-capacity Li metal anode, an Li–S battery that delivers up to (or possibly even more than) 400 W h kg^{-1} can be created. Li–S battery surpasses commercialized LIBs energy, but does not offer the cycling stability needed; <500 *vs.* >3000 cycles for LIBs [3–5]. The latter is mainly due to dissolution of reaction intermediates from the C/S electrode into the electrolyte. These are species with the general formula $(Li_2)S_n$ (n = 3–8), *e.g.* (lithium) polysulfides ((Li)PSs) that are formed during charge and discharge [6]. Their dissolution leads to loss of AM and hence both rapid capacity decay and low Coulombic efficiency [7,8].

Numerous studies have reported on many different strategies and new materials to improve both the (practical) energy density and the cycling stability [9–14] but relatively few have focused on understanding the very mechanisms underlying these phenomena – which can be complicated to assess. They do include, but are not limited to, simultaneous electrochemical and disproportionation reactions [15–17] which furthermore are still not completely identified and understood, and have also been demonstrated to be different dependent on the nature of the electrolyte. For example, electrolytes based on solvents with high donor numbers (DNs) promote the redox reactions of various species by stabilizing multiple PSs, most notably the $S_3^{\bullet-}$ radical, which is then the most stable and dominant intermediate [18–23]. In contrast, in low DN solvents, such as di-methyl ether (DME), S_4^{2-} is predominant, with $S_3^{\bullet-}$ being more or less completely absent [24]. The stabilization of $S_3^{\bullet-}$ in tetrahydrofuran (THF), di-methyl acetamide (DMA) and di-methyl sulfoxide (DMSO) is well-documented [25,26]. The presence of $S_3^{\bullet-}$ produces highly coloured blue solutions, as seen *e.g.* in ultramarine pigments, while PSs such as S_4^{2-} and S_6^{2-} result in yellow hue solutions [20,25]. The relative concentrations of $S_3^{\bullet-}$ is also dependent on the concentration of sulfur in the solution, the temperature, and the elemental sulfur to alkali metal ratio. Recently, a few groups have shown the importance of the $S_3^{\bullet-}$ radical in Li–S batteries and that it affects the

* Corresponding author.
E-mail address: roza.bouchal@mpikg.mpg.de (R. Bouchal).

https://doi.org/10.1016/j.powera.2024.100153
Received 29 February 2024; Received in revised form 21 May 2024; Accepted 16 June 2024
Available online 26 June 2024

electrochemical reduction of elemental sulfur and therefore is a key species in order to make possible the full utilization of both elemental sulfur and any Li_2S present [20,21]. The latter is affected as the ability of the electrolyte to stabilize the radical induces homogenous precipitation of Li_2S. Along these lines, Zhang et al. [22] reported that the high DN solvent tetra-methylurea (TMU) exhibits favourable Li_2S deposition kinetics and better compatibility towards lithium metal anodes than other high DN solvents [27]. Similar results were obtained using high DN anions, that preferentially induce 3D particle-like growth of Li_2S, while low DN anions result in a film-like morphology. The former effectively delayed electrode passivation and consequently led to high sulfur utilization [23]. In some contrast, Cuisinier et al., showed by using NMR spectroscopy that $S_3^{\bullet-}$ is reactive at elevated temperatures towards DOL, which is a common solvent in Li–S battery electrolytes, and this can possibly be held responsible for the capacity fading observed for extended Li–S battery cycling [20]. Another issue is that most high DN solvents, such as DMA, THF and DMSO, are corrosive towards lithium. Taken all together, it is not clear if $S_3^{\bullet-}$ is truly beneficial to Li–S battery cycling, nor whether or not it is promoting the full utilization of the AM.

To elucidate further on this, we here employ radical traps and primarily *operando* Raman spectroscopy to directly monitor the effect of $S_3^{\bullet-}$ on the Li–S battery capacity and cycling stability, using two different electrolytes: 1 M LiTFSI in either DME:DOL or TMU:DOL. The approach of radical or spin trapping is widely used in the fields of medical and organic chemistry [28,29]. Spin trapping is based on the acceptance of short-lived radicals by certain compounds (spin traps) with the formation of stable radicals (radical adducts) [30]. In this technique diamagnetic compounds called spin trapping agents, such as nitrone or nitroso, react with a free radicals to obtain a stable paramagnetic spin adduct. The nitrone (R–CH═NO-R') group is an important spin trap category where the radical is added to the adjacent carbon atom to the nitrone [31]. In contrast, the iminium cation was recently demonstrated to trap nucleophilic radicals. Melchiorre et al. reported on the enantioselective trapping of photochemically generated carbon-centered radicals [32,33]. The strong nucleophile character of $S_3^{\bullet-}$ [25] might thus render it effective with iminium cations. Inspired by this, we selected four molecules; two based on nitrone and two with iminium cations as our prospective $S_3^{\bullet-}$ traps. Two, *5,5-dimethyl-1-pyrroline-N-oxide* (**DMPO**) and *alpha-(4-Pyridyl N-oxide)-N-tert-butylnitrone* (**PotBN**), are widely used as nitrone radical traps, while the other two are ionic liquids (ILs) *1-ethyl-3-methyl-imidazolium bis(trifluoromethylsulfonyl)imide* and *1-butyl-3-methyl-pyridinium bis(trifluoromethylsulfonyl)imide*, which, for simplicity, henceforth will be referred to as **Emim** and **BmPyr**, respectively (Fig. S1). Note, ionic liquids have never previously been used as radical traps and were selected here due to their chemical, thermal and electrochemical stabilities. Using an $S_3^{\bullet-}$ radical trap in an Li–S battery while cycling is by no means trivial; the trap must be electrochemically and chemically stable toward all other battery components, selectively react solely with $S_3^{\bullet-}$, which is extra difficult as the electrolyte composition changes as (Li)PSs are formed, *i.e.* also as a function of the Li–S battery state-of-charge.

2. Experimental

2.1. Chemicals

Lithium bis(trifluoromethanesulfonyl)imide (LiTFSI, 99.95%) and 1-ethyl-3-methylimidazolium TFSI (EmimTFSI, 99.9%) were both purchased from Solvionic. 1-butyl-3-methylpyridinium TFSI (BmPyrTFSI, 99%) was purchased from Iolitec. 1,3-dioxolane (DOL) (anhydrous, 99.8% with 75 ppm butylated hydroxytoluene as inhibitor), di-methyl ether (DME, 99.9%), di-methyl acetamide (DMA) and tetra-methyl urea (TMU, 99%) were all obtained from Sigma-Aldrich. 1,2-(1,1,2,2-tetrafluoroethoxy) ethane (TFEE) was bought from Apollo Scientific. 5,5-Dimethyl-1-pyrroline-N-oxide (DMPO, ≥98%) and alpha-(4-pyridyl N-oxide)-N-tert-butyl-nitrone (PotBN, 99%) were both purchased from VWR. The Li foil (125 μm, 99.9%) was purchased from Cyprus Foote Mineral. The carbon/sulfur (C/S) composite electrodes were provided within the framework of the HELIS project from ISIT Fraunhofer and had 65% S loading on an aluminium current collector. Whatman glass fibre (GF/D, 675 μm) was used as separator.

2.2. Drying

LiTFSI was dried overnight at 120 °C under vacuum in a Buchi oven. All the solvents were dried before use. The solvents were in contact with activated 3 Å molecular sieves. After two days, the solvents were filtered out by using a 450 nm PTFE filter to remove any dust resulting from the sieves. The water content was checked by using Karl-Fischer titration and was found to be < 8 ppm. The C/S composite cathodes were dried at 45 °C under vacuum overnight.

2.3. Cell assembly and tests

2.3.1. For galvanostatic cycling tests

Coin-cells were made using an Li foil anode of 15 mm Ø and a C/S cathode of 13 mm Ø with a loading of 2.5 mg_S/cm^2 separated by a 16 mm Ø Whatman glass fiber separator holding 80 μl of electrolyte corresponding to a 24 $\mu l/mg_S$ E/S ratio. The galvanostatic cycling was performed using a Scribner battery cycler at room temperature between 1.5 and 2.8 V Li^+/Li° at a C/10 rate.

2.3.2. For the operando Raman spectroscopy

The Li–S batteries were assembled in a homemade *in situ* cell with a quartz window. 16 mm Ø C/S composite electrodes were used as cathodes and 18 mm Ø lithium discs as counter electrodes. The lithium foil was brushed to remove any surface layer and then pressed to obtain a homogeneous and smooth surface. Afterwards, a 2 mm Ø hole was made in the lithium disc. 1 Whatman separator (19 mm Ø) was used together with ca. 200 μl of electrolyte corresponding to a 38–40 μl/mg electrolyte to sulfur (E/S) ratio. Two electrolytes were used without and with four different traps (**Emim**, **PotBN**, **DMPO** and **BmPyr**): 1 M LiTFSI in DME: DOL (1:1, v:v) and 1 M LiTFSI in TMU: DOL (1:1, v:v). The quantity of trap in the electrolyte was equivalent to 0.78 mmol of nitrone/or iminium cation in 1 ml of electrolyte, which is 3.1 10^{-2} $mmol/mg_S$ nitrone/or iminium cation to sulfur ratio. The galvanostatic cycling was here performed using a Gamry Series G 300 galvanostat at room temperature between 1.8 and 2.8 V *vs.* Li^+/Li° at C/20 rate.

The assembly of all the above cells was done in an argon-filled glove box with an O_2 and H_2O content <1 ppm.

2.4. (Operando) Raman spectroscopy

The Raman spectra were collected at room temperature using a LabRAM Confocal Raman Spectrometer with a Peltier cooled CCD, equipped with a 632 nm laser operated at a power <4 mW on the sample surface, a 600 grooves/mm grating, and a pinhole size of 200 μm. The spectra were collected in backscattering geometry with a 10 × objective (confocal micro-Raman mode). To increase the signal-to-noise ratio (S/N), each spectrum is the average of 10 accumulations of 1 min each at a resolution of approximately 2 cm^{-1}. The focal plane was adjusted to be at the separator surface and very close to the edge of the hole in the Li anode, in order to reduce the effect of inhomogeneity of the electric field lines distribution. Spectral processing consisted essentially of removing spikes and background correction. The spectra from the *operando* experiments were normalized to the TFSI peak intensity at *ca.* 740 cm^{-1}.

2.5. SEM characterization

The Li metal anode foils were recovered from the above tests after 100 cycles, by disassembling the coin-cells inside the Ar-filled glovebox,

and by rinsing the foils with DME to remove any excess electrolyte. Subsequently, the foils were torn apart with tweezers to expose the cross-section and then transferred to the SEM in an airtight transfer chamber. The SEM was carried out using Carl Zeiss microscope at 3.0 kV acceleration voltage. Using the same airtight transfer chamber, the samples were transferred for XPS analysis. A PHI VersaProbeIII system employing a monochromatic Al Kα source (1486.6 eV) was used and the concentric hemispherical analyzer was positioned at 45° angle from the sample average.

3. Results and discussion

3.1. Solvent effects on the $S_3^{\bullet-}$ formation

Starting with proper $S_3^{\bullet-}$ radical formation identification, we apply open-circuit voltage (OCV) conditions and Raman spectroscopy using a home-made Raman cell presented in Fig. S2a. By focusing on the well-known $S_3^{\bullet-}$ peak at *ca.* 532 cm^{-1} [34], we find $S_3^{\bullet-}$ in all electrolytes, excepted the TFEE based, as previously reported (Fig. 1a (left) and Fig. S2b) [35–37]. The peak intensity and thus the concentration of $S_3^{\bullet-}$ follows TMU > TEGDME > DME (≫TFEE). These observations can be explained by $S_3^{\bullet-}$ being formed through disproportionation of the S_6^{2-} anion, why the solubility of Li_2S_6 in the electrolyte is an important property [27,38–40]. Indeed, the solubility of any Li-salt is usually lower in ether based electrolytes due to their low permittivity/dielectric constants (ε) [35–37,41]. TEGDME has a relative advantage *vs.* DME by its possibility of multidentate coordination by five (two) oxygen atoms and can thereby wrap around the Li^+ cation (Fig. 1b) [42,43]. In contrast, the fluorinated ether TFEE has fluorine atoms shielding the oxygen atoms, hindering effective coordination. The 74*X* cm^{-1} band of TFSI [44], often used to monitor cation-anion contact ion-pair formation between Li^+ and TFSI and thus clearly also being a function of the cation-solvent interaction [43], shifts towards higher frequencies as: TFEE > DME > TEGDME ≈ TMU (Fig. 1a (right)). A note in passing is that the latter spectrum shows two bands in this region, which may point to a different mode of interaction.

3.2. E/S ratio effects on the $S_3^{\bullet-}$ concentration

The $S_3^{\bullet-}$ radical concentration has been shown to increase as an inverse function of both electrolyte salt concentration and, what we focus on here, the elemental sulfur to lithium ratio [25,39,45]. First, we demonstrate that $S_3^{\bullet-}$ indeed can be monitored as a function of potential for a 1 M LiTFSI in DME:DOL electrolyte at an 18 E/S ratio (Fig. 2a). Please first note that, as opposed to what usually is the case, no $LiNO_3$ was added to the electrolyte, in order to avoid any possible interaction with $S_3^{\bullet-}$, and this explains the incomplete charge potential (due to PSs shuttling). Second, the intensity of $S_3^{\bullet-}$ in the spectra does (surprisingly) not change considerably for the different E/S ratios (Fig. 2b). The concentration of $S_3^{\bullet-}$ is, however, still somewhat lower in the electrolytes with the lower E/S ratios, *i.e.* 11.6 and 18, which likely is due to these cells' smaller electrolyte volumes, which result in higher PS concentrations.

3.3. Trapping effects on the $S_3^{\bullet-}$ concentration

Moving on to the very trapping itself, a solution of 0.2 mM Li_2S_6 in DMA – a high DN solvent known to stabilize $S_3^{\bullet-}$ – gave a by the eye blue solution (Fig. S3) and subsequent addition of traps changed the colour; **Emim** turned it transparent, both **PotBN** and **BmPyr** turned it yellow, and **DMPO** made it light blue-green. The latter could be due to **DMPO**'s sensitivity to water, it may have decomposed and hence be less effective to trap $S_3^{\bullet-}$. The Raman spectra of the solutions are shown in Figs. S4 and S5. Initially, the solution containing 0.2 mM Li_2S_6 in DMA was compared with both dilute 0.04 mM Li_2S_6 in DMA and with DMA solvent alone. The peak related to $S_3^{\bullet-}$ at 532 cm^{-1} increase with the Li_2S_6 concentration, along with two other peaks at 1062 and 1594 cm^{-1}. The latter two peaks are associated with the solvation of DMA to $S_3^{\bullet-}$. Furthermore, Fig. S5 shows the spectra of traps in DMA with and without 2 mM Li_2S_6. The spectra clearly show that the change related to the presence of traps in Li_2S_6 in the DMA solution is only associated to the three peaks assigned to $S_3^{\bullet-}$ radical and to its solvation by DMA. The peak at 537 ± 1 cm^{-1} in **PotBN** and **BmPyr** is not related to $S_3^{\bullet-}$ as it is present in the solutions without Li_2S_6. However, a slight increase in intensity and peak position shift to 533 cm^{-1} is observed in **PotBN** added to 0.2 mM Li_2S_6 in DMA solution, while in **Bmpyr** stayed unchanged. Furthermore, the peak below 1110 cm^{-1} is slightly altered in all traps, which might be related to either DMA solvent or traps. Regarding the peaks associated with polysulfides (PSs), it is important to note that these peaks often overlap with those of the DMA solvent. However, for **PotBN**, there is a slight increase in these peaks, suggesting a potential alteration in PS concentration.

Turning to the *operando* Raman spectroscopy studies, we now use two different electrolytes with low and high DN solvents: 1 M LiTFSI in DME:DOL and in TMU:DOL, respectively. For reference, the full Raman spectra of the different traps in both electrolytes are presented in Fig. S6. The traps show to have an effect on both the discharge capacity and the $S_3^{\bullet-}$ peak area (Fig. 3 and Figs. S7 and 8). For the DME based electrolyte

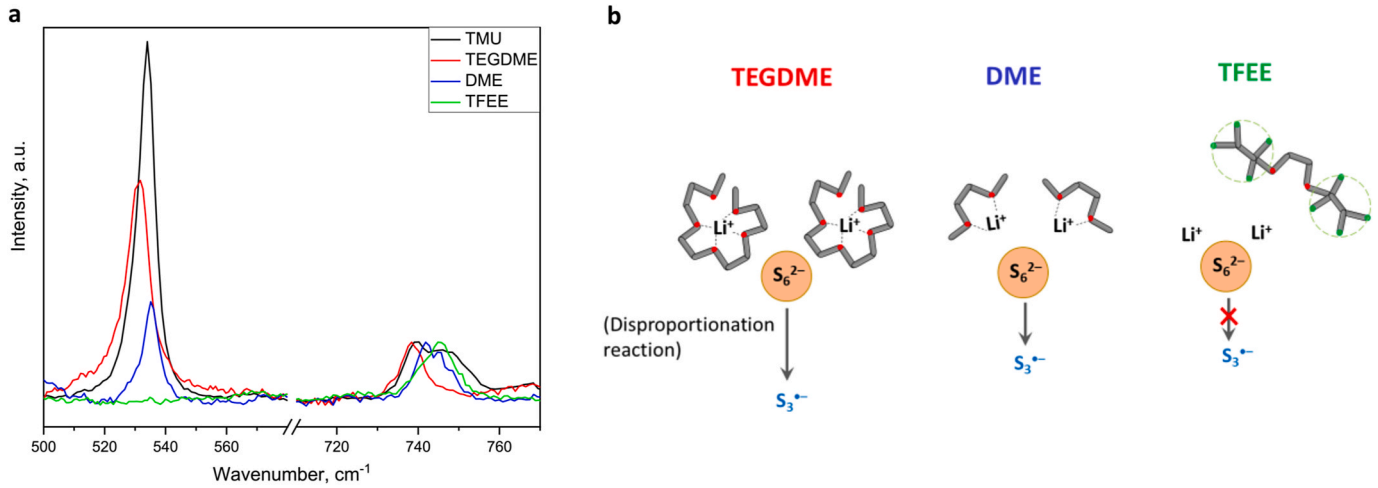

Fig. 1. Li^+, TFSI and $S_3^{\bullet-}$ interactions: a) Raman spectra of different electrolytes under OCV conditions in selected $S_3^{\bullet-}$ and TFSI regions, and b) Schematic representations of the Li^+ solvation hypotheses for different ether based electrolytes and the consequences for $S_3^{\bullet-}$ formation.

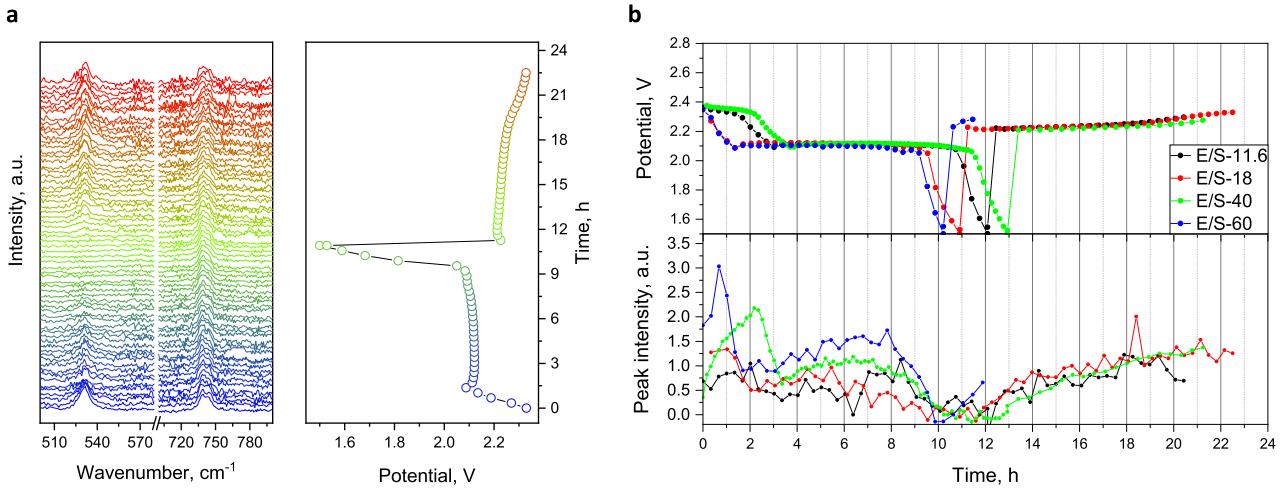

Fig. 2. The effect of E/S ratio on $S_3^{\bullet-}$ *radical concentration: a)* Operando *Raman spectra upon cycling using a 1 M LiTFSI in DME:DOL electrolyte at a 18 E/S ratio, and b) Peak areas of* $S_3^{\bullet-}$ *upon cycling using different E/S ratios.*

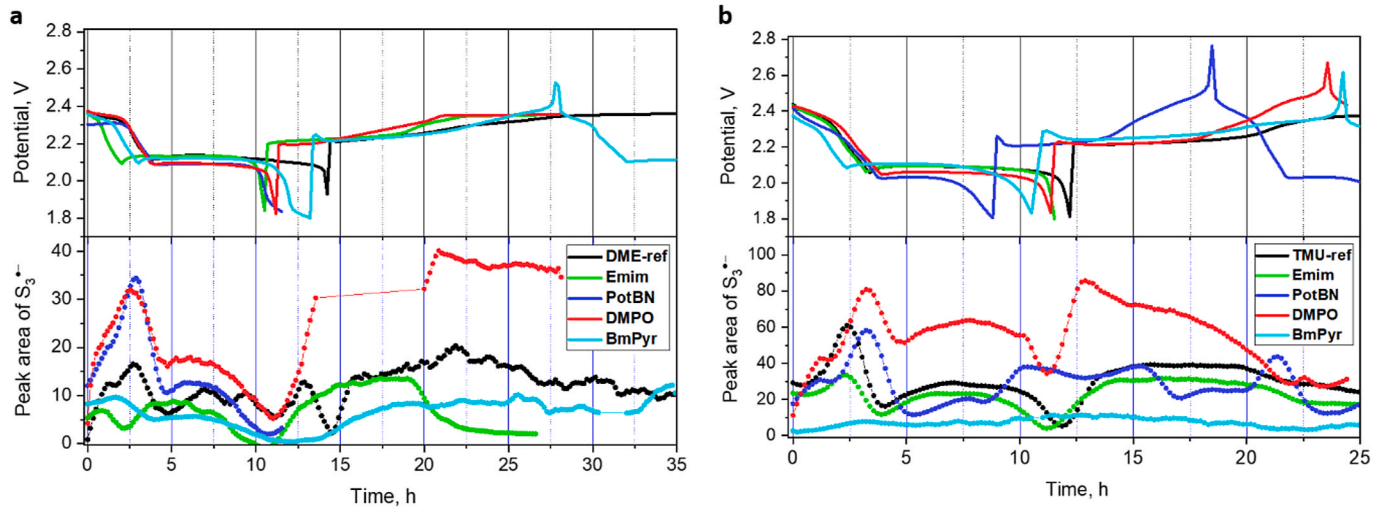

Fig. 3. Operando *Raman experimental data showing potential profiles along the evolution of* $S_3^{\bullet-}$ *peak areas: a) 1 M LiTFSI in DME:DOL, and b) 1 M LiTFSI in TMU:DOL.*

(Fig. 3a and Fig. S7), all the traps reduce the discharge capacity, but only **BmPyr** reduces the shuttling effect. **PotBN** and **DMPO** both reduce only the second plateau capacity, in contrast to **Emim** and **BmPyr**. Surprisingly, however, both **DMPO** and **PotBN** increase the $S_3^{\bullet-}$ peak area, especially at the beginning of both discharge and charge, in contrast to both **Emim** and **BmPyr**. This is in stark contrast to what was observed for **DMPO** and **PotBN** in the *ex situ* experiments, why we believe that **DMPO** and **PotBN** undergo irreversible electrochemical reactions during the cycling [46]. We observe almost the same tendency in the TMU based electrolyte (Fig. 3b and Fig. S8), wherein particularly **BmPyr** reduces the $S_3^{\bullet-}$ peak area to *ca.* 1/6th.

Furthermore, as $S_3^{\bullet-}$ usually appears on the slope after the first plateau [22,27,39,47], which also corresponds to the formation of S_6^{2-} [47], the trapping effect should be larger at the beginning of discharge, before the first slope. For both electrolytes, both **Emim** and **BmPyr** reduce the discharge capacity of the first plateau and at the same time decrease the $S_3^{\bullet-}$ peak area, and **BmPyr** has a larger effect on the TMU based electrolyte, which has a higher $S_3^{\bullet-}$ concentration.

3.4. Trap effects on the PS formation

To further understand the effect of the traps, we thoroughly investigated the PS formation in the presence of **Emim** and **BmPyr**. The individual assignment of different PSs from the Raman spectra is somewhat ambiguous, but general correlations with the potential profiles can nevertheless be made.

3.4.1. DME based electrolyte

For the DME-based electrolyte without any trap added, the Raman spectra (Fig. 4a and Fig. S9a) are in agreement with the literature; the first discharge plateau corresponds to the formation of long-chain PSs as a result of the S_8 ring opening [48,49], the two peaks at 369 and 398 cm^{-1} are assigned to $S_{7,8}^{2-}$ and S_6^{2-}, respectively [50–53]; and a broad peak around 490 cm^{-1} found at the beginning of the first discharge plateau is assigned to different S_n^{2-} (n = 4–8) species [51,54,55]. The latter peak shifts to 485 cm^{-1} indicating the reduction to short-chain PSs such as S_4^{2-} which is also mainly contributing at 445 cm^{-1} [51,52,56–59]. $S_3^{\bullet-}$ is observed at 532 cm^{-1} [25,45,50–52,56], a feature of which the intensity reduces along the discharge similarly to the S_6^{2-} feature. All these peak intensities decrease until completely vanishing at

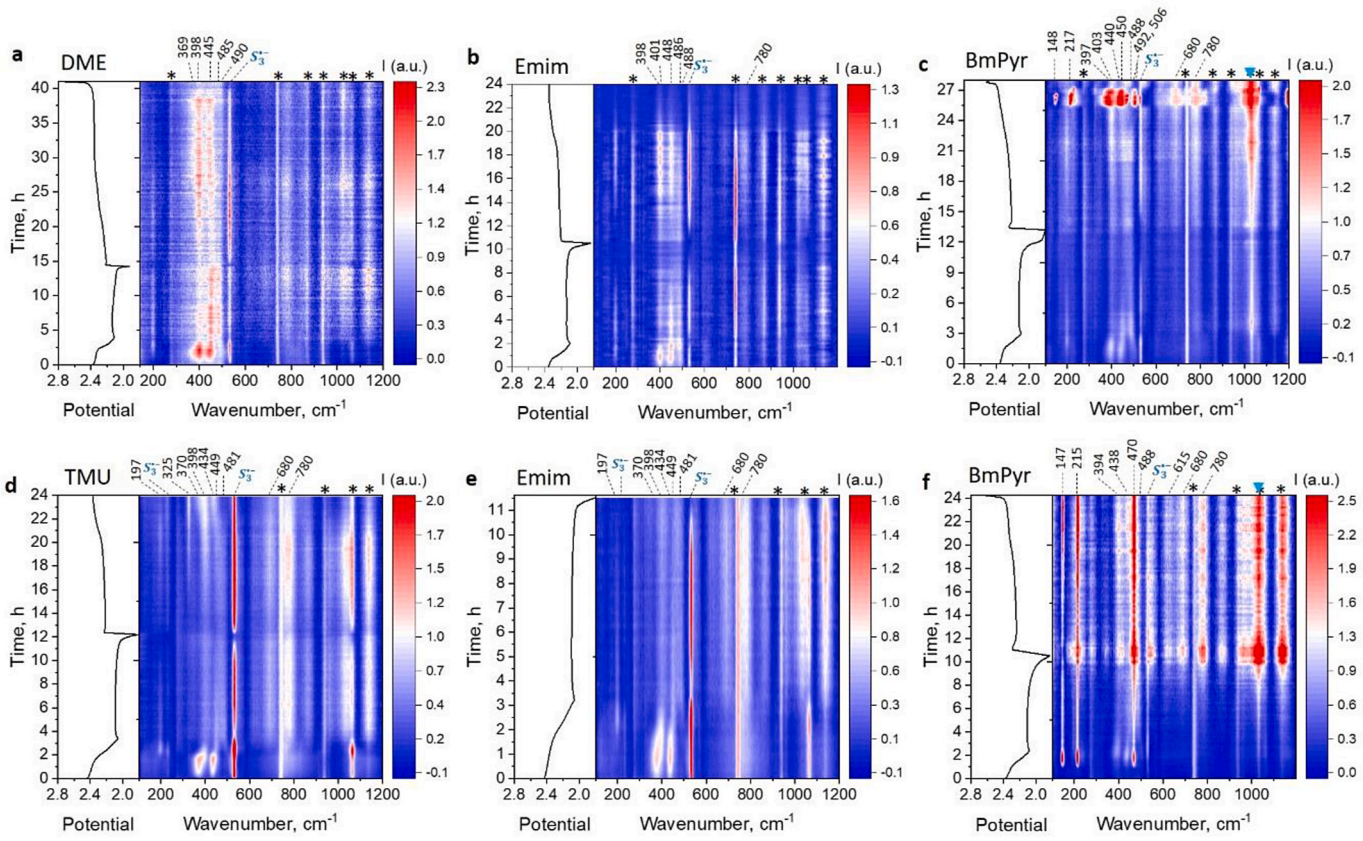

Fig. 4. Operando Raman spectra as heatmaps for a Li–S battery cell including the potential profile of the C/S composite cathode at C/20 rate: a) 1 M LiTFSI in DME:DOL, b) Emim in 1 M LiTFSI in DME:DOL, c) BmPyr in 1 M LiTFSI in DME:DOL, d) 1 M LiTFSI in TMU:DOL, e) Emim in 1 M LiTFSI in TMU:DOL and f) BmPyr in 1 M LiTFSI in TMU:DOL. star = electrolyte, triangle = trap.

the end of the discharge. The reappearance of the peaks during charge clearly shows the reversibility.

The addition of **Emim** changes the Raman spectra slightly (Fig. 4b and **S9b**); long PSs are found as peaks at 488 and 398 cm^{-1}, which shift during cycling to 486 and 401 cm^{-1}, respectively, corresponding to the reduction to short-chain PSs [50,51]. In addition, S_6^{2-} mainly contributes at 398 cm^{-1} at the beginning of the discharge process [50,52,53]. The peak at 448 cm^{-1} is assigned mainly to S_4^{2-} [51,56,58–60]. The $S_3^{\bullet-}$ peak can be observed, but with a lower intensity, especially during the first slope. This shows that **Emim** does not completely inhibit the radical during cycling and that there are mainly short-chain PSs present in the electrolyte. The addition of **BmPyr** results in a slightly different pattern of spectra and spectral changes (Fig. 4c and S9c). The presence of long-chain PSs is observed at the beginning of the discharge process. The two overlapping peaks at 492 and 506 cm^{-1} are attributed to long-chain PSs (S_{6-8}^{2-}) [36,54–56] but they shift and become one peak at 488 cm^{-1} starting from the second plateau, corresponding to the reduction of long-chain to short-chain PSs. S_6^{2-} can be observed at 397 cm^{-1} and similarly shifts to 403 cm^{-1}, which can be assigned to $S_{4,5}^{2-}$ [36,51,61]. Another peak is observed in the 1st plateau at 440 cm^{-1} and shifts slightly to 450 cm^{-1}, which is indicative of long-chain PSs reduction to S_4^{2-} [51,56,58–60].

3.4.2. *TMU based electrolyte*

As expected, the TMU based electrolyte spectra show a very different PSs evolution (Fig. 4d and **S10a**). In the beginning of the discharge process, we mainly observe two peaks at 370 and 434 cm^{-1}, respectively, whose intensities increase during the first plateau and which are assigned to long-chain PSs S_{6-8}^{2-} [8,50,51], but also $S_{4,5}^{2-}$ may contribute to the latter [51,55,61]. These two peaks' intensities reach their maxima just before the first slope, whereafter they decrease while shifting positions to 398 and 446 cm^{-1}, respectively, which indicates reduction to S_6^{2-} (398 cm^{-1}) [50–53] and S_4^{2-} (446 cm^{-1}) [36,56,61]. At the beginning of the second plateau, we observe formation of short-chain PSs at 449 cm^{-1} (S_4^{2-}), 481 cm^{-1} ($S_{4,5}^{2-}$) [58] and 197 cm^{-1} (S_4^{2-}) [57,59,61,62], but these peaks are not very well defined. During the charging process, we observe peak shifts indicating formation of long-chain PSs at 396 cm^{-1} [52,54,56]. However, as mentioned before, full cell charging was not reached because of the shuttling effect, which might explain the peak at 438 cm^{-1} assigned to S_n^{2-} (n = 4–8) [8,50,51]. In addition to the peak formation at 325 cm^{-1} corresponding to S_3^{2-} [63], the $S_3^{\bullet-}$ radical can be observed at 530 and 230 cm^{-1} [45,52,64]. We also observe that the intensity of the TMU peak at 1062 cm^{-1} follows the peak intensity of $S_3^{\bullet-}$, which indicates solvation of $S_3^{\bullet-}$ by TMU. Similarly to the *ex situ* Raman analysis in DMA-based solutions.

Surprisingly, the electrolyte Raman spectra with the **Emim** trap added show the same evolution during the discharge as the reference electrolyte (Fig. 4e and **S10b**). However, despite the same PSs formation, the $S_3^{\bullet-}$ peak intensity is only slightly lower during the first discharge plateau and slope. In stark contrast, when **BmPyr** was added, the Raman spectra in Fig. 4f and **S10c** revealed an entirely different trend; at the beginning of the discharge process, three peaks related to PSs can be observed at 394, 438, and 488 cm^{-1}. The first is associated to long-chain PSs (S_8^{n-} (n = 1–2)and S_7^{2-}) [50–53], while the two latter are new and may be assigned to both short- and long-chain PSs [8,50,51,55]. Furthermore, in the middle of the first discharge plateau, three strong peaks appears at 147, 215 and 470 cm^{-1}, the latter attributed to S_4^{2-} or S_3^{2-} [61,63,65], but the two former are (again) new. In addition, the absence of any peak at 325 cm^{-1} discards the possibility of S_3^{2-}. The peaks at 394 and 438 cm^{-1} increase in the intensity during the first

discharge plateau, then shift to 402 and 445 cm^{-1} and decrease in intensity during the first slope – indicating reduction of long-chain to short-chain PSs. The weak peak at 489 cm^{-1}, assignable to short-chain PSs, undergoes a broadening and shifts towards higher wavenumbers; maximum to 505 cm^{-1}, which might indicate ring opening of S_8 to S_8^{2-} and S_7^{2-} [52,54,55], and then back to 488 cm^{-1} during the first discharge slope. Finally, a new peak appeared at 780 cm^{-1} at the beginning of the charge, which may indicate interaction between **BmPyr** and $S_3^{\bullet-}$, similarly as seen for the DME based electrolyte [66].

From all of the above, we can conclude that despite the different effects of **BmPyr** in the TMU and DME based electrolytes, it clearly alters the PS formation in both electrolytes. **Emim**, on the other hand, seems to have only a slight impact on the PS formation and the $S_3^{\bullet-}$ concentration, especially in the TMU based electrolyte. While it is still unclear *how* both **Emim** and **BmPyr** interact with $S_3^{\bullet-}$ and/or the other PSs, the decreased $S_3^{\bullet-}$ peak intensity in the **BmPyr** based electrolytes can nevertheless be indicative of a different PS formation pathway.

The plausible role of $S_3^{\bullet-}$: a literature study

Previously, it was shown that $S_3^{\bullet-}$ can assist long PS species to reduce to shorter PSs. Cuisinier et al. [47], showed that the $S_3^{\bullet-}$ radical plays a key intermediate role in a set of reactions (Equations (1)–(3) below) before ultimately being reduced to solid-state Li_2S. Similarly, Gupta et al. [21], proposed that the presence of $S_3^{\bullet-}$ avoids the early precipitation of Li_2S and allows the full utilization of S_8.

$$S_3^{\bullet-} + e^- \rightarrow S_3^{2-} \quad (1)$$

$$2S_3^{\bullet-} + 2S_3^{2-} \rightarrow 2S_4^{2-} \quad (2)$$

$$S_8^{2-} + 2e^- \rightarrow 2S_4^{2-} \quad (3)$$

Cuisinier et al. [47], proposed that in high DN solvents, any sulfur species formed via electrochemical reduction (such as S_2^{2-} or S_1^{2-}) must equilibrate with leftover oxidized species (S_8 or S_8^{2-}) to form more stable intermediates ($S_3^{\bullet-}$ or S_{3-4}^{2-}; Equation (4)). The latter drives the full consumption of S_8, and prevents the early precipitation of Li_2S in the presence of long-chain PSs.

$$S_1^{2-} + 1/4S_8 \rightarrow S_3^{2-} \quad (4)$$

According to a recent study by He et al. [67], using a DME based electrolyte, the meta-stable PS S_3^{2-} is also formed during discharge and quickly disproportionate to S_4^{2-} and Li_2S_2/Li_2S. This explains why S_3^{2-} is not observed by *ex situ* characterization. The intermediate S_3^{2-} enhances the capacity and lengthen the second discharge plateau as the reaction requires 5 e^- to form the Li_2S_2/Li_2S precipitates. According to equations (5)–(9), they suggested that the conversion of S_8 to S_4^{2-} and then to S_3^{2-} are fast processes, while the capacity extraction from S_3^{2-} to form Li_2S is limiting the discharge rate in DOL:DME-based Li–S batteries.

$$S_4^{2-} + 2/3e^- \rightarrow 4/3S_3^{2-} \quad (5)$$

$$S_3^{2-} + 4e^- \rightarrow 3S_1^{2-} \quad (6)$$

$$S_3^{2-} + 1e^- \rightarrow 3/2S_2^{2-} \quad (7)$$

$$2S_3^{2-} \leftrightarrow S_4^{2-} + S_2^{2-} \quad (8)$$

$$3S_3^{2-} \leftrightarrow 2S_4^{2-} + S_1^{2-} \quad (9)$$

Similar to He et al.'s research, our *in situ* Raman spectroscopy data do not reveal any presence of S_3^{2-} in the DME based electrolyte. It is, however, observed at 325 cm^{-1} in the TMU based electrolyte during the charging step. This could be explained by the possibility of high donor number solvents stabilizing S_3^{2-} and/or to the large amount of $S_3^{\bullet-}$ radical formed during charging process. However, this peak vanishes when **BmPyr** is added. Furthermore, the second discharge plateau was shortened in the presence of **BmPyr** trap in both DME and TMU based electrolytes. Although S_3^{2-} is observed during charge in TMU based electrolyte, the decrease in the discharge capacity might be explained by the suppression of Equation (1), which hinders the formation of S_3^{2-}. However, the mechanism in the DME based electrolyte is less clear, as the formation of S_3^{2-} arises from the reduction of S_4^{2-}, as indicated by Equation (6). We hold the view that the possibility of a minor presence of $S_3^{\bullet-}$ in the DME based electrolyte could plausibly stimulate the formation of S_3^{2-}. Notably, the investigation by He et al. categorically excludes any existence of $S_3^{\bullet-}$.

Despite the complexity of the system, our findings are in line with the literature. We showed in direct way that $S_3^{\bullet-}$ trapping alters significantly the PSs formation. The meta-stable PS S_3^{2-}, dependent on $S_3^{\bullet-}$ formation, might be the important intermediate for the full utilization of sulfur.

3.5. Effects of the tri-sulfur radical on the capacity and cycling stability

To correlate all the above spectroscopic findings with Li–S battery performance, we set out to study the effects of the different traps on the cycling stability using coin-cell batteries (with slightly lower E/S ratios (24 μl/mg_S) as compared to the *operando* cells to more mimic "real" cells). Again, as there is no $LiNO_3$ additive in any of the electrolytes, PSs shuttling effects have large impact, why a capacity limit was applied to the DME reference electrolyte.

The effects of the **Emim** trap on cycling stability and potential profiles are different in the DME and the TMU based electrolytes (Fig. 5). For the former, the capacity decreases continuously for the first 20 cycles and then stabilizes alongside improved Coulombic efficiency (Fig. 5a). The reduced capacity comes mainly from the second discharge plateau (Fig. S11). For the TMU based electrolyte, however, **Emim** improves both the capacity and the Coulombic efficiency of the first 40 cycles (Fig. 5b). Here, in stark contrast, the improved capacity comes from the second discharge and first charge plateau (Fig. S12). A similar trend was observed in the *operando* Raman spectra, where a different PSs formation was observed only for the DME based electrolyte. **Emim** clearly has different effects depending on the electrolyte solvent employed and therefore this cannot be directly linked to $S_3^{\bullet-}$ radical trapping, but rather inferred to either Emim's solvation in the electrolyte or possible interactions with other PSs.

Both **PotBN** and **DMPO**, however, show similar effects for the DME and TMU based electrolytes. For the former electrolyte, they both decrease the long-term capacity, while for the latter trap the initial capacity increases using the TMU based electrolyte (Fig. S13), but levels off after ca. 30 cycles, while the Coulombic efficiency is slightly improved by both traps. Thus a **DMPO** induced increase of $S_3^{\bullet-}$ concentration can improve both the initial capacity (Fig. S12) and Coulombic efficiency.

On the other hand, the addition of **BmPyr**, to both DME and TMU based electrolytes, reduces the capacity and significantly alters the potential profiles – resulting in cell failure after only 20–25 cycles (Fig. 5), alongside a distinctly different PSs pathway, in particular at the start of the first slope and at the start of the charge, which corresponds to the $S_3^{\bullet-}$ formation. The same effect is observed for the TMU based electrolytes (Fig. S12); the overpotential is increased, the first discharge plateau potential is lower, the first slope is longer, and the second discharge plateau disappears. During the charging process, the first plateau is almost absent; the potential is close to the second plateau potential. While our findings are in agreement with previous studies showing the importance of $S_3^{\bullet-}$ stabilization for full AM utilization [22,23], the low $S_3^{\bullet-}$ concentration in the DME based electrolyte makes any unambiguous statement on its importance for capacity and stability difficult. It is, however, very clear that the PSs formation in the DME based electrolyte is less altered as compared to in the TMU based electrolyte.

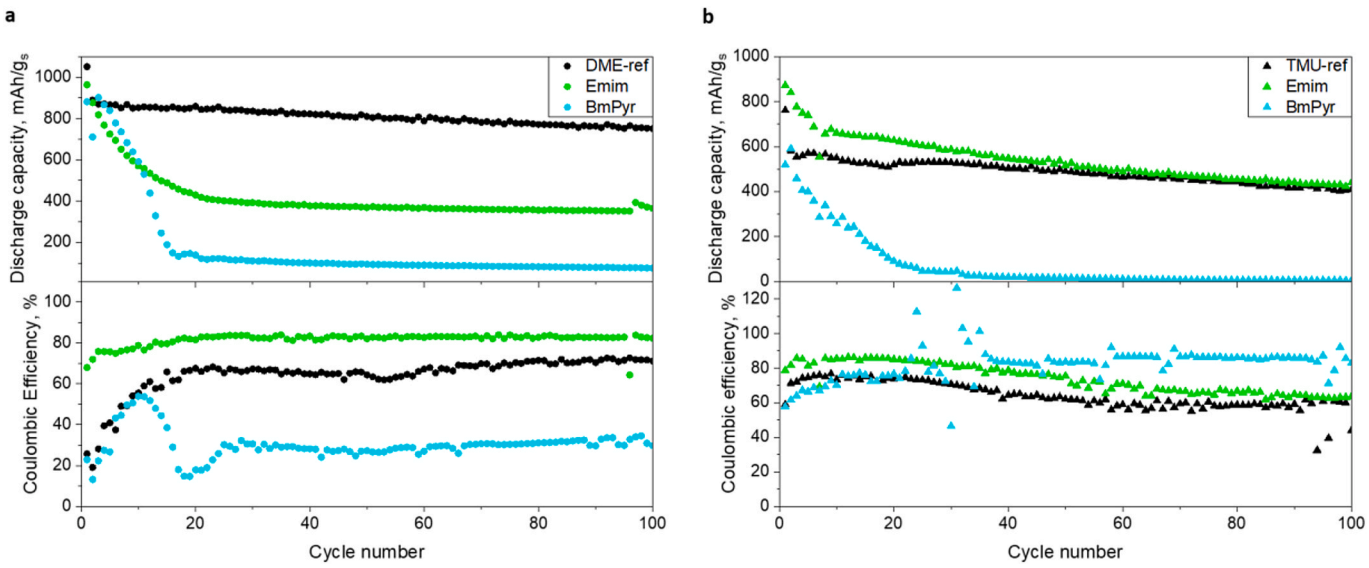

Fig. 5. Effects of **Emim** and **BmPyr** traps on cycling stability by discharge capacity and Coulombic efficiency of: a) DME and b) TMU based electrolytes.

3.6. *Lithium anode stability in the presence of $S_3^{\bullet-}$ traps*

To further qualify the prospective role(s) of the traps, the stability of the Li metal anode was also investigated, especially with respect to any dendrite formation. The cross-section SEM micrographs of Li foils recovered after approx. 100 cycles show serious detoriation in the DME reference electrolyte case (Fig. 6a and **b**), which is in agreement with the literature [68]. Detoriation is still visible when the **Emim**, **PotBN**, and **DMPO** traps are added to the electrolyte (Fig. S14), but for **BmPyr** added there are only a few small particles that can be observed on the surface, which can be detached Li (Fig. 6c and **d**). The TMU based electrolytes exhibit somewhat different characteristics but show similar trends; almost all show dendrite formation, excepted the electrolyte with the **BmPyr** trap added. Both the TMU reference electrolyte and the one with **PotBN** added show less detoriation than when the **Emim** or **DMPO** traps were added (Fig. S15). They differ between a whiskers-like [69] Li growth for the TMU reference electrolyte to cracks for the **PotBN** trap added. In contrast, with the **Emim** trap added the Li foil display globular shaped deposits. Finally, using **BmPyr** render a denser surface and unchanged thickness and thus **BmPyr** stabilizes the surface of Li anode (why the observed cell cycling failures must be related rather to the changes in the PS formation).

The composition of the SEI layers formed on Li metal anodes were further investigated by X-ray photoelectron spectroscopy (XPS). For DME based electrolytes in Fig. S16, the spectra show almost similar composition with and without traps excepted for the **PotBN** trap. However, the intensity and ratio of the different elements change with the added traps. The C1s spectra present the commonly observed species, including C–C (~284.8 eV), C–O (~285.7 eV) and CO_3^{2-} (~289.3 eV) [70–72]. C–F groups can be observed only for the DME reference electrolyte, while the **PotBN** trap added demonstrate a higher contribution of COOR at 288.3 eV even as compared to the C–C groups. The carbonate-based compounds are also confirmed in the O1s and Li1s surveys. In addition, the **PotBN** sample shows an additional peak at 535 eV which is related to poly(CO_3) [70,72] from solvent or **PotBN** decomposition. However, the presence of Li–N–C at 402.8 eV [72,73] and 58.4 eV[72] in N1s and Li1s surveys, respectively, might indicate the **PotBN** decomposition instead. C–F and Li–F groups can be observed at

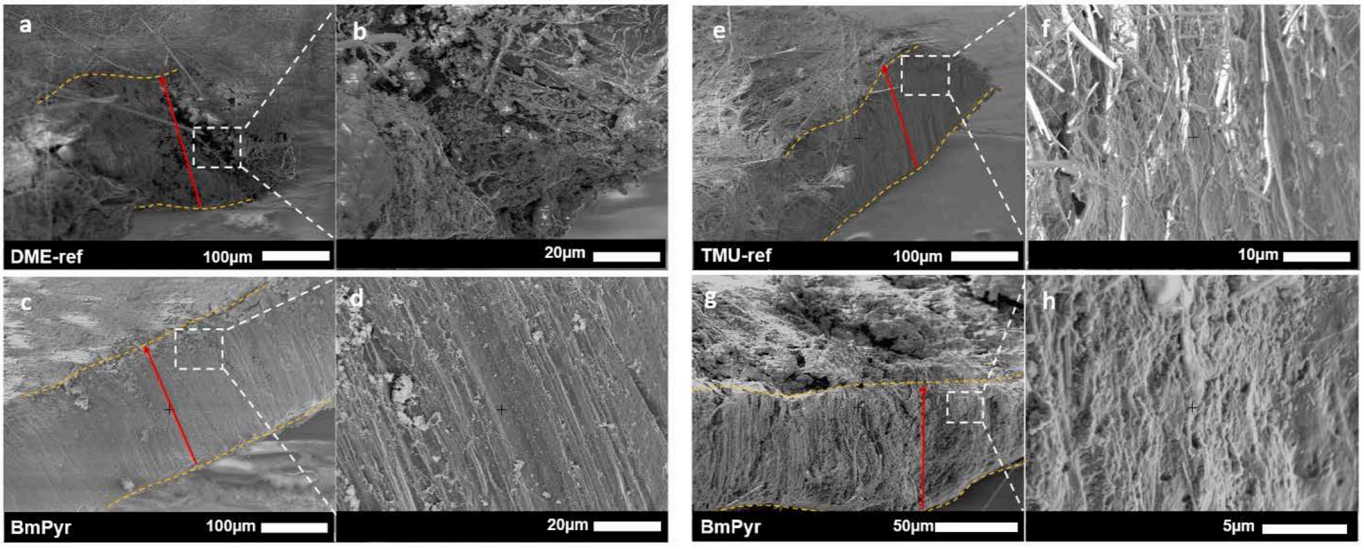

Fig. 6. Cross-section SEM micrographs of recovered lithium metal anodes after cycling: a, b) Reference DME based electrolyte; c, d) DME based electrolyte with **BmPyr**; e, f) Reference TMU based electrolyte; and g, h) TMU based electrolyte with **BmPyr**.

688.8 eV and 685 eV in all electrolytes, except in **PotBN** which displays only C–F group with an additional peak at 692 eV which might be assigned to SF group [74,75]. These results might indicate an interaction of **PotBN** or it is a decomposition by-product with PSs. LiF is further confirmed in the different electrolytes in Li1s survey, while it is absent in the **PotBN** sample in accordance to the F1s survey. The **BmPyr** shows a shift to lower binding energy which might indicate the presence of Li metal, but also LiO_2 or Li–OH as demonstrated in the O1s survey. $LiSO_2F$ from the TFSI anion can be observed at 171 and 170 eV together with sulfate, polythionate, sulfone and sulfonate [76]. Similarly, these compounds are confirmed at 401 eV and 399 eV, related to N-SO_x and Li_xN [72]. However, the added traps displays the presence of short PSs at 160 eV and 162 eV. Sulfone might also contribute at 162 eV, while longer PSs such as S_8 are observed at 164 eV [76,77]. Although the added traps shows at lower intensity of TFSI compound than PSs, Table S1 demonstrate similar amount of sulfur in all electrolytes, indicating higher content of oxygen and fluorine in DME reference electrolyte. While the other electrolytes display lower content of fluorine, especially **BmPyr** which indicate higher content of carbon. Overall, the results shows an SEI composition of both organic and inorganic compounds and their changes depending on the added trap.

For TMU-based electrolytes, almost similar compositions were observed, the C1s spectra show the presence of C–C and C–O in TMU reference electrolyte, the latter peak is increased in **Emim** added-trap, while **BmPyr** and **DMPO** show a new peak at 288 eV indicated the presence of higher amount of carbonate compounds. These compounds are confirmed by the O1s survey where there is clearly an additional peak related to C–O–C and poly(CO_3) [71,72]. However, **BmPyr** trap added did not demonstrate the presence of carbonate at Li1s. The S2p survey displays for all electrolytes both TFSI by-products: sulfate, polythiofane and sulfonate, as well as PSs (Li_2S, Li_2S_2 and S_8) [76]. Although the peak of S_8 is more pronounced in the **BmPyr** sample, Table S1 shows that there is a lower percentage of elemental sulfur in comparison to the other electrolytes. C–F and Li–F compounds were observed in all electrolytes, however, these peaks intensity are very low wheni the **BmPyr** trap has been added (Table S1). The peak at 692 eV assigned previously to SF was observed only in **DMPO** which might indicate the impact of solvent on **DMPO** interaction or decomposition processes. Finally, the **BmPyr** added shows one sharp peak at Li1s at 56.8 eV which was attributed to LiF. As the peak is sharp, in addition to lower amount of F in comparison to Li (*see* Table S2) the contribution of plated Li^0 can also be considered.

To conclude the composition of the SEI in both DME and TMU based electrolytes is of organic and inorganic compounds. The decomposition of **PotBN** and **DMPO** can be confirmed in DME and TMU solvent, respectively. The **Emim** trap demonstrated almost similar composition products as the reference electrolyte, expected the sulfur compounds. Finally, **BmPyr** shows a composition of more organic compounds while the presence of more Li is higher in comparison to other elements. These results indicate that the SEI composition should not alter the cell stability. Furthermore, **BmPyr** can be suggested as a good SEI additive for Li metal anodes.

4. Concluding remarks

By employing radical traps and *operando* Raman spectroscopy, we have monitored the effect of the $S_3^{\bullet-}$ radical on the PS formation, battery capacity and stability. First, we confirmed the $S_3^{\bullet-}$ concentration dependence on type of solvent and E/S ratio. Second, different traps based on nitrone and iminium cation were investigated with respect to their ability to trap $S_3^{\bullet-}$ as well as the formation of $S_3^{\bullet-}$ in low and high DN solvent based electrolytes. By this, we managed to successfully trap $S_3^{\bullet-}$ using **BmPyr**, which results in decreased battery capacity and cell failure after only a few cycles. Moreover, a different PS formation was observed during $S_3^{\bullet-}$ trapping in both DME and TMU based electrolytes. Our results confirm, in agreement with the literature, the impact of $S_3^{\bullet-}$ in and on different Li–S electrolytes, which is important information for future Li–S battery (electrolyte) development. However, further work is still needed to elucidate more exactly *how* the $S_3^{\bullet-}$ trapping changes the PS formation pathway and impacts Li–S battery performance.

CRediT authorship contribution statement

Roza Bouchal: Writing – review & editing, Writing – original draft, Visualization, Validation, Methodology, Investigation, Formal analysis, Data curation, Conceptualization. **Clément Pechberty:** Investigation. **Athmane Boulaoued:** Methodology, Investigation. **Niklas Lindahl:** Investigation. **Patrik Johansson:** Writing – review & editing, Validation, Supervision, Resources, Investigation, Conceptualization.

Declaration of competing interest

The authors declare that they have no known competing financial interests or personal relationships that could have appeared to influence the work reported in this paper.

Data availability

Data will be made available on request.

Acknowledgement

The European Commission provided financial support for this work within the project “High-Energy Lithium–Sulfur Cells and Batteries” (HELIS) under research grant agreement No. 666221.

Appendix A. Supplementary data

Supplementary data to this article can be found online at https://doi.org/10.1016/j.powera.2024.100153.

References

[1] M.A. Weret, W.N. Su, B.J. Hwang, Strategies towards high performance lithium-sulfur batteries, Batter. Supercaps 5 (2022) e202200059.
[2] J. Ma, et al., The 2021 battery technology roadmap, J. Phys. D Appl. Phys. 54 (2021) 183001.
[3] Y. Chen, et al., Advances in lithium–sulfur batteries: from academic research to commercial viability, Adv. Mater. 33 (2021) 2003666.
[4] M. Ue, K. Sakaushi, K. Uosaki, Basic knowledge in battery research bridging the gap between academia and industry, Mater. Horiz. 7 (2020) 1937–1954.
[5] S. Urbonaite, T. Poux, P. Novák, Progress towards commercially viable Li–S battery cells, Adv. Energy Mater. 5 (2015) 1500118.
[6] J. Scheers, S. Fantini, P. Johansson, A review of electrolytes for lithium–sulphur batteries, J. Power Sources 255 (2014) 204–218.
[7] S. Drvarič Talian, J. Moškon, R. Dominko, M. Gaberšček, Reactivity and diffusivity of Li polysulfides: a fundamental study using impedance spectroscopy, ACS Appl. Mater. Interfaces 9 (2017) 29760–29770.
[8] J.D. McBrayer, T.E. Beechem, B.R. Perdue, C.A. Apblett, F.H. Garzon, Polysulfide speciation in the bulk electrolyte of a lithium sulfur battery, J. Electrochem. Soc. 165 (2018) A876–A881.
[9] G. Zheng, Y. Yang, J.J. Cha, S.S. Hong, Y. Cui, Hollow carbon nanofiber-encapsulated sulfur cathodes for high specific capacity rechargeable lithium batteries, Nano Lett. 11 (2011) 4462–4467.
[10] Y. Yang, et al., New nanostructured Li2S/Silicon rechargeable battery with high specific energy, Nano Lett. 10 (2010) 1486–1491.
[11] S. Xin, et al., Smaller sulfur molecules promise better lithium'sulfur batteries, J. Am. Chem. Soc. 134 (2012) 18510–18513.
[12] D. Lin, et al., Layered reduced graphene oxide with nanoscale interlayer gaps as a stable host for lithium metal anodes, Nat. Nanotechnol. 117 11 (2016) 626–632, 2016.
[13] X. Liang, et al., A highly efficient polysulfide mediator for lithium–sulfur batteries, Nat. Commun. 61 (6) (2015) 1–8, 2015.
[14] X. Ji, K.T. Lee, L.F. Nazar, A highly ordered nanostructured carbon–sulphur cathode for lithium–sulphur batteries, Nat. Mater. 8 (2009) 500–506.
[15] Y. Lu, Q. He, H.A. Gasteiger, Probing the Lithium – Sulfur Redox Reactions: A Rotating-Ring Disk Electrode Study. **5741**, 2014.

[16] Y. Gorlin, et al., Understanding the charging mechanism of lithium-sulfur batteries using spatially resolved operando X-ray absorption spectroscopy, J. Electrochem. Soc. 163 (2016) A930–A939.
[17] A.T.S. Freiberg, et al., Species in lithium-sulfur batteries using spatially resolved operando X-ray absorption spectroscopy and X-ray fluorescence mapping, J. Phys. Chem. C 122 (2018) 5303–5316.
[18] Q. Zou, Y.C. Lu, Solvent-dictated lithium sulfur redox reactions: an operando UV-vis spectroscopic study, J. Phys. Chem. Lett. 7 (2016) 1518–1525.
[19] K.H. Wujcik, et al., Characterization of polysulfide radicals present in an ether-based electrolyte of a lithium-sulfur battery during initial discharge using in situ X-ray absorption spectroscopy experiments and first-principles calculations, Adv. Energy Mater. 5 (2015) 1500285.
[20] M. Cuisinier, C. Hart, M. Balasubramanian, A. Garsuch, L.F. Nazar, Radical or not radical: revisiting lithium-sulfur electrochemistry in nonaqueous electrolytes, Adv. Energy Mater. 5 (2015) 1401801.
[21] A. Gupta, A. Bhargav, A. Manthiram, Highly solvating electrolytes for lithium–sulfur batteries, Adv. Energy Mater. 9 (2019) 1803096.
[22] G. Zhang, et al., The radical pathway based on a lithium-metal-compatible high-dielectric electrolyte for lithium–sulfur batteries, Angew. Chem. 130 (2018) 16974–16978.
[23] H. Chu, et al., Achieving three-dimensional lithium sulfide growth in lithium-sulfur batteries using high-donor-number anions, Nat. Commun. 10 (2019) 188.
[24] M. Cuisinier, et al., Sulfur speciation in Li-S batteries determined by operando X-ray absorption spectroscopy, J. Phys. Chem. Lett. 4 (2013) 3227–3232.
[25] T. Chivers, P.J.W. Elder, Ubiquitous trisulfur radical anion: fundamentals and applications in materials science, electrochemistry, analytical chemistry and geochemistry, Chem. Soc. Rev. 42 (2013) 5996.
[26] T. Chivers, Ubiquitous trisulphur radical ion S3-, Nature 252 (1974) 32–33.
[27] Q. Wang, et al., Direct observation of sulfur radicals as reaction media in lithium sulfur batteries, J. Electrochem. Soc. 162 (2015) A474–A478.
[28] P. Maillard, C. Giannotti, Utilisation des pièges à radicaux en vue de mettre en évidence des intermédiaires dans la photolyse de complexes contenant une liaison Co III —C, Can. J. Chem. 60 (1982) 1402–1413.
[29] R.P. Mason, Imaging free radicals in organelles, cells, tissue, and in vivo with immuno-spin trapping, Redox Biol. 8 (2016) 422–429.
[30] C.C. Rowlands, D.M. Murphy, Chemical applications of EPR, Encycl. Spectrosc. Spectrom. (2017) 173–179, https://doi.org/10.1016/B978-0-12-803224-4.00139-4.
[31] K. Manzoor, Detection and Analysis of Spin Trapped Radical Adducts Using Thermal Desorption Gas Chromatography Mass Spectrometry (TD-GC-MS), 2018.
[32] J.J. Murphy, D. Bastida, S. Paria, M. Fagnoni, P. Melchiorre, Asymmetric catalytic formation of quaternary carbons by iminium ion trapping of radicals, Nat 532 (2016) 218–222, 2016 5327598.
[33] A. Bahamonde, et al., Studies on the enantioselective iminium ion trapping of radicals triggered by an electron-relay mechanism, J. Am. Chem. Soc. 139 (2017) 4559–4567.
[34] T. Chivers, C. Lau, Raman spectroscopic identification of the S4N- and S3- ions in blue solutions of sulfur in liquid ammonia, Inorg. Chem. 21 (1982) 453–455.
[35] S. Drvarič Talian, et al., Fluorinated ether based electrolyte for high-energy lithium-sulfur batteries: Li+Solvation role behind reduced polysulfide solubility, Chem. Mater. 29 (2017) 10037–10044.
[36] R. Bouchal, et al., Monitoring polysulfide solubility and diffusion in fluorinated ether-based electrolytes by operando Raman spectroscopy, Batter. Supercaps 3 (2020) 397–401.
[37] M. Gao, et al., A high performance lithium–sulfur battery enabled by a fish-scale porous carbon/sulfur composite and symmetric fluorinated diethoxyethane electrolyte, J. Mater. Chem. A 5 (2017) 6725–6733.
[38] B. Zhang, et al., The fundamental understanding of lithium polysulfides in ether-based electrolyte for lithium-sulfur batteries, ACS Energy Lett. 6 (2021) 537–546.
[39] R. Steudel, T. Chivers, The role of polysulfide dianions and radical anions in the chemical, physical and biological sciences, including sulfur-based batteries, Chem. Soc. Rev. 48 (2019) 3279–3319.
[40] X. Han, X. Xu, Mechanistic insights into trisulfur radical generation in lithium–sulfur batteries, J. Mater. Chem. A 11 (2023) 18922–18932.
[41] S. Jeschke, P. Johansson, Predicting the solubility of sulfur: a COSMO-RS-based approach to investigate electrolytes for Li–S batteries, Chem. Eur J. 23 (2017) 9130–9136.
[42] P. Johansson, J. Tegenfeldt, J. Lindgren, Modelling amorphous lithium salt–PEO polymer electrolytes: ab initio calculations of lithium ion–tetra-, penta- and hexaglyme complexes, Polymer (Guildf). 40 (1999) 4399–4406.
[43] L. Lutz, et al., High capacity Na−O 2 batteries: key parameters for solution-mediated discharge, J. Phys. Chem. C 120 (2016) 50.
[44] I. Rey, et al., Spectroscopic and theoretical study of (CF3SO2)2N- (TFSI-) and (CF3SO2)2NH (HTFSI), J. Phys. Chem. A 102 (1998) 3249–3258.
[45] T. Chivers, I. Drummond, Characterization of the trisulfur radical anion S3- in blue solutions of alkali polysulfides in hexamethylphosphoramide, Inorg. Chem. 11 (1972). https://pubs.acs.org/sharingguidelines.
[46] E. Braxton, et al., Electron paramagnetic resonance for the detection of electrochemically generated hydroxyl radicals: issues associated with electrochemical oxidation of the spin trap, ACS Meas. Sci. Au (2022), https://doi.org/10.1021/ACSMEASURESCIAU.2C00049.
[47] M. Cuisinier, C. Hart, M. Balasubramanian, A. Garsuch, L.F. Nazar, Radical or not radical: revisiting lithium-sulfur electrochemistry in nonaqueous electrolytes, Adv. Energy Mater. 5 (2015) 1–6.
[48] L. Zhang, et al., In situ optical spectroscopy characterization for optimal design of lithium-sulfur batteries, Chem. Soc. Rev. 48 (2019) 5432–5453.
[49] M. Wild, et al., Lithium sulfur batteries, a mechanistic review, Energy Environ. Sci. 8 (2015) 3477–3494.
[50] J. Hannauer, et al., The quest for polysulfides in lithium-sulfur battery electrolytes: an operando confocal Raman spectroscopy study, ChemPhysChem 16 (2015) 2755–2759.
[51] M. Hagen, et al., In-situ Raman investigation of polysulfide formation in Li-S cells, J. Electrochem. Soc. 160 (2013) A1205–A1214.
[52] J.J. Chen, et al., Conductive lewis base matrix to recover the missing link of Li2S8 during the sulfur redox cycle in Li-S battery, Chem. Mater. 27 (2015) 2048–2055.
[53] R. Steudel, Y. Steudel, Polysulfide chemistry in sodium-sulfur batteries and related systems- A computational study by G3X(MP2) and PCM calculations, Chem. Eur J. 19 (2013) 3162–3176.
[54] T. Chivers, F. Edelmann, J.F. Richardson, K.J. Schmidt, Convenient synthesis, X-ray crystal structure, and Raman spectrum of the heptasulphide dianion, S72-, in [PPN]2S7·2EtOH, Can. J. Chem. 64 (1986) 1509–1513.
[55] R. Steudel, F. Schuster, Normalschwingungen und Rotationsisomerie von Polysulfidionen Sn2-(n = 4 — 8), Z. Naturforsch. A Phvs. Chem. Kosmophys. 32 (1977) 1313–1319.
[56] W. Zhu, et al., Investigation of the reaction mechanism of lithium sulfur batteries in different electrolyte systems by: in situ Raman spectroscopy and in situ X-ray diffraction, Sustain. Energy Fuels 1 (2017) 737–747.
[57] A. Ward, Raman spectrum and force constants of S42, Mater. Res. Bull. 4 (1969) 581–590.
[58] G.J. Janz, et al., Raman studies of sulfur-containing anions in inorganic polysulfides. Sodium polysulfides, Inorg. Chem. 15 (1976) 1759–1763.
[59] H. Hermann, G. Wieghardt, H. Kleinschmager, G. Weddigen, Raman and IR spectra of solid alkalimetalpolysulfides, Z. Naturforsch. 31 (1976) 415–418.
[60] O. El Jaroudi, E. Picquenard, A. Demortier, J.P. Lelieur, J. Corset, Polysulfide anions II: structure and vibrational spectra of the S42- and S52- anions. Influence of the cations on bond length, valence, and torsion angle, Inorg. Chem. 39 (2000) 2593–2603.
[61] G.J. Janz, J.W. Coutts, J.R. Downey, E. Roduner, Raman studies of sulfur-containing anions in inorganic polysulfides. Potassium polysulfides, Inorg. Chem. 15 (1976) 1755–1759.
[62] J. Wang, et al., Low-temperature and high-rate Zn metal batteries enabled by mitigating Zn2+ concentration polarization, Chem. Eng. J. 433 (2022) 134589.
[63] H. Wieser, P.J. Krueger, E. Muller, J.B. Hyne, Vibrational spectra and a force field for H_2S_3 and H_2S_4, Can. J. Chem. 47 (1969) 1633–1637.
[64] H.L. Wu, L.A. Huff, A.A. Gewirth, In situ Raman spectroscopy of sulfur speciation in lithium-sulfur batteries, ACS Appl. Mater. Interfaces 7 (2015) 1709–1719.
[65] P. Dubois, J.P. Lelieur, G. Lepoutre, Identification and characterization of lithium polysulfides in solution in liquid ammonia, Inorg. Chem. 27 (1988) 73–80.
[66] P. Bazylewski, R. Divigalpitiya, G. Fanchini, In situ Raman spectroscopy distinguishes between reversible and irreversible thiol modifications in l -cysteine, RSC Adv. 7 (2017) 2964–2970.
[67] Q. He, A.T.S. Freiberg, M.U.M. Patel, S. Qian, H.A. Gasteiger, Operando identification of liquid intermediates in lithium–sulfur batteries via transmission UV–vis spectroscopy, J. Electrochem. Soc. 167 (2020) 080508.
[68] A. Basile, A.I. Bhatt, A.P. O'Mullane, Stabilizing lithium metal using ionic liquids for long-lived batteries, Nat. Commun. 71 (7) (2016) 1–11, 2016.
[69] L. Frenck, G.K. Sethi, J.A. Maslyn, N.P. Balsara, Factors that control the formation of dendrites and other morphologies on lithium metal anodes, Front. Energy Res. 7 (2019) 115.
[70] J. Zheng, et al., Highly stable operation of lithium metal batteries enabled by the formation of a transient high-concentration electrolyte layer, Adv. Energy Mater. 6 (2016) 1502151.
[71] H. Yu, et al., Dendrite-free lithium deposition with self-aligned columnar structure in a carbonate-ether mixed electrolyte, ACS Energy Lett. 2 (2017) 1296–1302.
[72] Q. Wang, et al., Interface chemistry of an amide electrolyte for highly reversible lithium metal batteries, Nat. Commun. 111 11 (2020) 1–11, 2020.
[73] A. Basile, A.I. Bhatt, A.P. O'Mullane, Stabilizing lithium metal using ionic liquids for long-lived batteries, Nat. Commun. 71 (7) (2016) 1–11, 2016.
[74] J. Li, et al., Weak cation–solvent interactions in ether-based electrolytes stabilizing potassium-ion batteries, Angew. Chem. Int. Ed. 61 (2022) e202208291.
[75] R. Miao, et al., A new ether-based electrolyte for dendrite-free lithium-metal based rechargeable batteries, Sci. Rep. 61 (6) (2016) 1–9, 2016.
[76] M.J. Lacey, et al., The Li–S battery: an investigation of redox shuttle and self-discharge behaviour with LiNO3-containing electrolytes, RSC Adv. 6 (2016) 3632–3641.
[77] T. Liu, et al., Low-density fluorinated silane solvent enhancing deep cycle lithium–sulfur batteries' lifetime, Adv. Mater. 33 (2021) 2102034.